

## Thermal and electrochemical analysis on SnSO<sub>3</sub>/ZnSO<sub>3</sub> nanocomposite

R. Gayathri<sup>a</sup>, S. Shanmugha Soundare<sup>b</sup>, M. Mithren<sup>a</sup>,  
S. Aripnammal<sup>a,\*</sup>

<sup>a</sup> *Department of Physics, Gandhigram Rural Institute, Deemed To Be University, Gandhigram-624302, Dindigul District, Tamilnadu, India*

<sup>b</sup> *Centre for Nanoscience and Technology, Anna University, Chennai-600025, Tamilnadu, India*

SnSO<sub>3</sub>/ZnSO<sub>3</sub> nanocomposite is synthesized by hydrothermal method. X-ray powder diffraction assures perfect formation of nanocomposite. It reveals morphology of nail like nanorod structure. Thermal analysis illustrates the sample's thermal behavior. X-ray photoemission analysis describes the chemical state of Zn, Sn, S and O in SnSO<sub>3</sub>/ZnSO<sub>3</sub>. Electrochemical study in three electrode system, exhibits voltammogram of bell-shaped curve. Operational potential window is 1.6 V. Chronopotentiometry depicts the quasi-triangular curves, demonstrating pseudocapacitor behavior. Specific capacitances at 1 A/g current density is 117.8 F/g. Nyquist plot for SnSO<sub>3</sub>/ZnSO<sub>3</sub> assures pseudocapacitor behavior and suggests that the system is found to be stable.

(Received January 7, 2025; Accepted March 17, 2025)

*Keywords:* SnSO<sub>3</sub>/ZnSO<sub>3</sub>, Thermal, X-ray photoemission, Electrochemical studies

### 1. Introduction

In the modern era of technology, the utilization of nanoscale materials has grown with its evolved significance. Their potential roles include energy storage batteries, supercapacitors, photovoltaic, and photocatalysis, detecting process, in the discipline of biophysics, medicine, and catalysis. In addition to this, some proven examples of nanostructured electrode materials are porous semiconductors, polymeric nanocomposites, and fused nanoporous metallic oxides [1]. Researchers are exclusively paying attention on materials with nanoscale dimensions to develop effective energy-storage systems of all kinds. Nanoscale materials have several advantageous views, due to their large particle volume and rapid ion dispersion, such as enhanced electrical conductivity, which tends to produce high current, and high surface area ratio, which improves the efficiency of energy storage devices [2]. As an emerging view, oxychalcogenide materials play its presence over the limit with many exciting properties under nanoscale level. Usually, oxychalcogenide materials combines with any of the metals, to yield metal oxychalcogenides with alternative arrangement of oxide and chalcogenide anion with the metal cations. The studies on the metal oxychalcogenide nanocomposite shows numerous interesting properties due to imperfections on lattice plane. Researchers hope metal oxychalcogenide with the imperfections in the lattice plane are widely employed for energy storage applications, thermal catalysis, electro catalysis and photocatalysis. Moreover, all the enhanced technologies need renewable energy source for eco-friendly environment. To analyze the energy storing ability of materials, electrochemical approach is a potent method and widely employed for analysis. This study exists as vital resource for investigating electron transfer-initiated reactions [3]. This electrochemical technique is employed widely in modern analytical chemistry to characterize electro active species, as well as to determine the stability of oxidation states and the rate of electron transfer between the electrode and analytes [4-6]. This paper deals with the electrochemical and thermal analytical studies of SnSO<sub>3</sub>/ZnSO<sub>3</sub> nanocomposite. The doping effect of zinc and tin over sulphur favors more investigations relating to energy storing capabilities.

---

\* Corresponding author: aripnammal@gmail.com  
<https://doi.org/10.15251/JOR.2025.212.187>

## 2. Methods and materials

The nanocomposite  $\text{SnSO}_3/\text{ZnSO}_3$  was synthesized by hydrothermal technique [7]. The sample is characterized by X-ray powder diffraction (XRD), thermal analysis, x-ray photo emission spectroscopy (XPS) and electrochemical analysis. The Carel ZEISSEVO-18 model is used for recording SEM, Panalytical X'Pert Pro model for recording XRD with  $\text{Cu K}\alpha$  radiation, Thermo Fisher Scientific's XPS device for recording XPS spectra using  $\text{Al K}\alpha$  radiation (1486.6 eV), thermal analysis by NETZSCH make NJA-STA2500 Regulus model with Proteus software in the temperature range of  $30^\circ$  to  $800^\circ\text{C}$  and Bio-Logic VSP potentiostat model for doing electrochemical experiments.

The electrochemical performance of the synthesized  $\text{SnSO}_3/\text{ZnSO}_3$  electrode was evaluated in a three-electrode cell arrangement. A mixture of  $\text{SnSO}_3/\text{ZnSO}_3$ , carbon black, and PVDF was taken in a mortar and pestle and mixed well with few drops of NMP solution (N-methylpyrrolidone) in order to evaluate the electrochemical performance of  $\text{SnSO}_3/\text{ZnSO}_3$ . This slurry mixture was then applied to a  $1\text{ cm}^2$  Ni foam, which was then dried. In this work, 3M KOH electrolyte was utilized. Here, platinum wire serves as the counter electrode,  $\text{Ag}/\text{AgCl}$  serves as reference electrode, and Ni foam coated with substance serves as the working electrode.

## 3. Results and discussion

### 3.1. XRD

XRD Pattern of  $\text{SnSO}_3/\text{ZnSO}_3$  nanocomposite is shown in Figure 1. The peak values are identified and it confirms the crystalline nature of the composite.

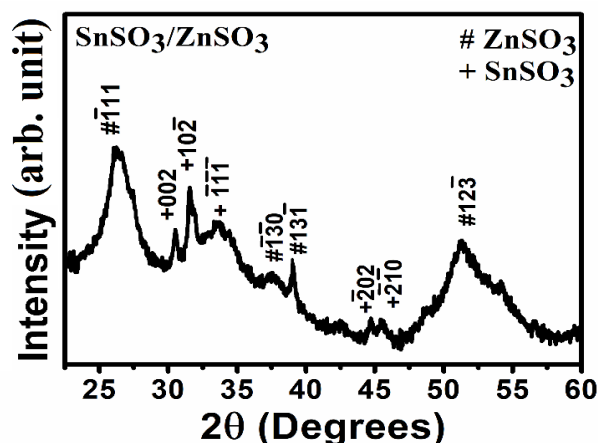


Fig. 1. XRD of  $\text{SnSO}_3/\text{ZnSO}_3$  nanocomposite.

Lattice parameters of  $\text{SnSO}_3$  are found to be  $a = 4.474\text{ \AA}$ ,  $b = 5.295\text{ \AA}$ , and  $c = 6.266\text{ \AA}$  [8] and for  $\text{ZnSO}_3$   $a = 4.320\text{ \AA}$ ,  $b = 8.622\text{ \AA}$ , and  $c = 6.440\text{ \AA}$  for  $\text{ZnSO}_3$  [9]. Both are of monoclinic structure. The absence of alloy peak points and fluctuations in graph indicate the existence of nano composite  $\text{SnSO}_3/\text{ZnSO}_3$  [10].

### 3.2. Surface morphological studies

Figure 2 depicts SEM picture of  $\text{SnSO}_3/\text{ZnSO}_3$  at 15 KX magnification. It exhibits sharp nail like nano rod structure.

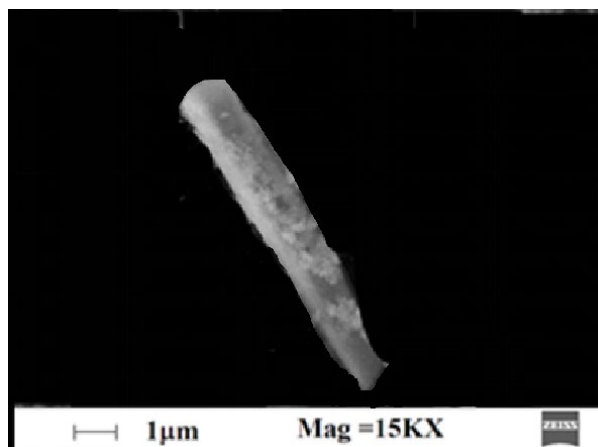


Fig. 2. SEM image of  $\text{SnSO}_3/\text{ZnSO}_3$  nanocomposite.

### 3.3. Thermo gravimetric analysis (TGA)

Figure 3 shows TGA curve of  $\text{SnSO}_3/\text{ZnSO}_3$ . The TGA curve represents the percentage of weight remaining as the sample when heated. The x-axis corresponds to temperature (in degrees Celsius), ranging from approximately 25°C to nearly 1000°C [11]. The left y-axis shows TG (%), indicating how much percentage of mass remains as temperature increases with values range from 70% to 100%.

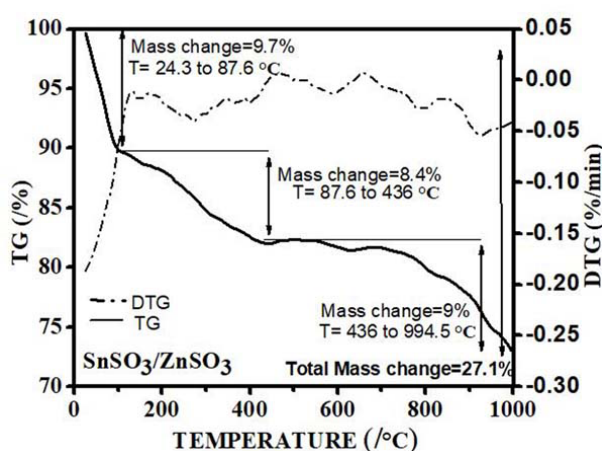


Fig. 3. TGA plot of  $\text{SnSO}_3/\text{ZnSO}_3$ .

It is observed that the mass change of 9.7% occurs from 24.3°C to 87.6°C, 8.4% of mass change occurs with the temperature ranging from 87.6°C to 436°C. With the efficient rise of temperature from 436°C to 995°C, drastic mass change is noted as 9%. The total mass change occurred is about 27.1%. The composite has appreciable mass loss around 88°C, which might be related to get rid of water molecules embedded into its structure. Further loss upto 436 °C, might be due to the carbonization or polymer reduction process. Beyond 436° C, the composite start decomposes drastically [12].

The differential thermo gravimetric (DTG) curve plots the rate of weight loss per minute versus temperature. Peaks on the DTG curve correlate to temperatures with a substantial shift in the rate of decrease in mass. These peaks represent rapid decrease in weight caused by particular thermal processes such as breakdown and phase transitions [12]. The TGA curve displays the sample's heat stability and breakdown characteristics. The DTG peaks indicate key temperatures at which

considerable weight loss occurs. The general outline implies different phases of disintegration or volatilization.

### 3.4. Differential thermal analysis (DTA)

Figure 4 depicts DTA curve of  $\text{SnSO}_3/\text{ZnSO}_3$ . The x-axis shows temperature in degrees Celsius ( $^{\circ}\text{C}$ ), ranging from  $0^{\circ}\text{C}$  to  $1000^{\circ}\text{C}$ . The y-axis shows difference in temperature (DTA signal) measured in milli watt per milligram ( $\text{mW}/\text{mg}$ ). At lower temperatures up to around  $100^{\circ}\text{C}$ , the curve appears flat with slight shifts. This suggests no significant thermal events during this range [12].

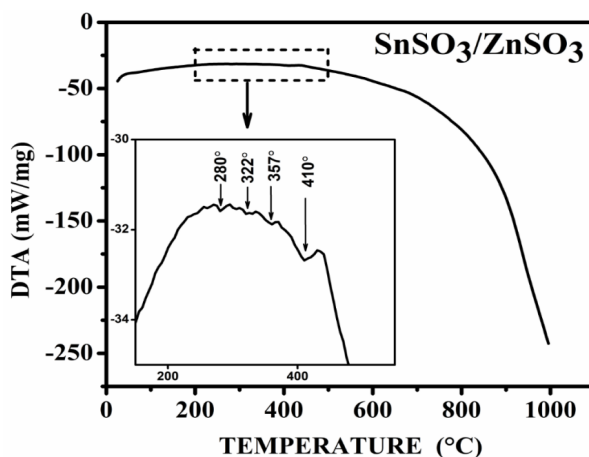


Fig. 4. DTA curve of  $\text{SnSO}_3/\text{ZnSO}_3$  nanocomposite.

Few troughs have been observed at  $280^{\circ}$ ,  $322^{\circ}$ ,  $357^{\circ}$  and  $410^{\circ}\text{C}$ . The trough at  $280^{\circ}$  likely corresponds to a thermal event in the sample which may be due to phase transition, such as crystallization or polymorphic transformation. It may also be due to chemical reaction due to the occurrence of decomposition, oxidation etc. The troughs at  $322^{\circ}\text{C}$  and  $357^{\circ}\text{C}$ , which are showing almost similar and tiny dip in the graph signifies a minute change in its transition. Suppose, if the sample contains crystalline regions, this could be the melting point. It might also indicate other transitions such as glass transition and recrystallization. The dip at  $410^{\circ}\text{C}$  could be another phase transition e.g., solid-solid transition or it may be any chemical reactions occur at this temperature. Beyond  $500^{\circ}\text{C}$ , the curve gradually slopes downward. This suggests an endothermic process where the sample absorbs heat by melting or decomposition. The DTA graph provides insights into material behavior under varying temperatures [13].

### 3.5. X-ray photo emission spectroscopy

The XPS spectrum is relevant for analyzing the surface chemistry and chemical binding state of materials. Here, nanocomposite  $\text{SnSO}_3/\text{ZnSO}_3$  is analyzed through XPS Spectrum. This material could be a layered compound or a composite containing both tin sulphite and zinc sulphite. The XPS peaks help to characterize the individual element in the compound [14].

Figure 5 shows tin 3d scan of  $\text{SnSO}_3/\text{ZnSO}_3$  nanocomposite. The Sn  $3d_{5/2}$  orbital can be identified by the peak at lower binding energy, which is approximately 487.0 eV. It stands for the energy needed to extract an electron from a tin atom's third subshell. The location of this peak reveals the details on the tin's chemical environment within the substance. The Sn  $3d_{3/2}$  orbital is shown by the peak at greater binding energy, which is approximately 495.8 eV [15]. The spin-orbit splitting between these components ( $\Delta$ ) is approximately 8.75 eV

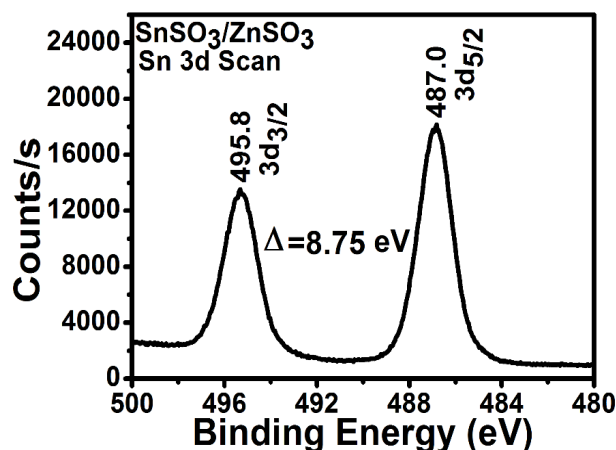


Fig. 5. Tin 3d scan of SnSO<sub>3</sub>/ZnSO<sub>3</sub>.

Figure 6 shows XPS of Zn in SnSO<sub>3</sub>/ZnSO<sub>3</sub> which explains the chemical state. The peaks in the zinc scan represent the 2p energy level of zinc (Zn). The Zn oxidation state can be inferred from the binding energy of the peaks. The increased intensity indicates that there is a significant quantity of zinc present in the substance. The binding energy of zinc's 2p electrons is represented by the Zn 2p peak. Zn 2p<sub>3/2</sub> and Zn 2p<sub>1/2</sub> are the two spin-orbit components that are usually visible. The peak point at 1022.3 eV corresponds to Zn 2p<sub>3/2</sub> with significant proof from previous literature survey. The binding energy of the Zn 2p<sub>1/2</sub> peak is somewhat greater at 1045.5 eV. These components have a spin-orbit splitting of about 23.2 eV [16]. Zinc oxide is said to have peaks at 1022.25 and 1045.31 eV [16-17], verifying that the sample contains a Zn oxide matrix [17].

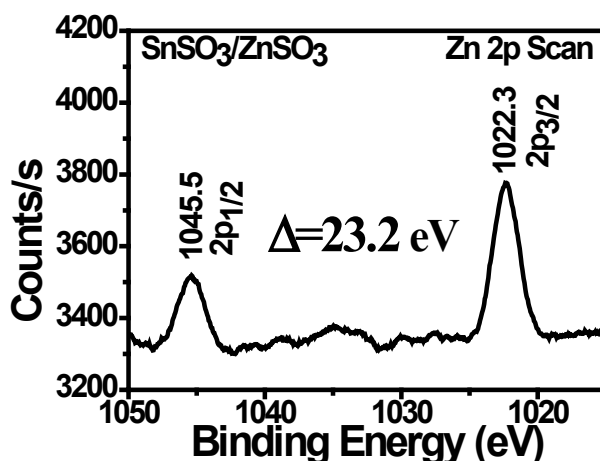


Fig. 6. Zinc 2p scan of SnSO<sub>3</sub>/ZnSO<sub>3</sub>.

The Figure 7 depicts S 2p spectrum confirming the presence of S by the occurrence of 2p<sub>1/2</sub> and 2p<sub>3/2</sub> peaks at BEs of 168.6 and 161.8 eV. According to a consistent literature investigation, the binding energy of pure sulphur is 164 eV, which changes depending on the chemical compound bonded to it [18]. The sulphur spectrum at 168.6 is occurred due to its higher oxidation state. Peak at 161.8 in the S 2p spectrum correspond to photoelectrons from reduced sulfur groups [19-20]

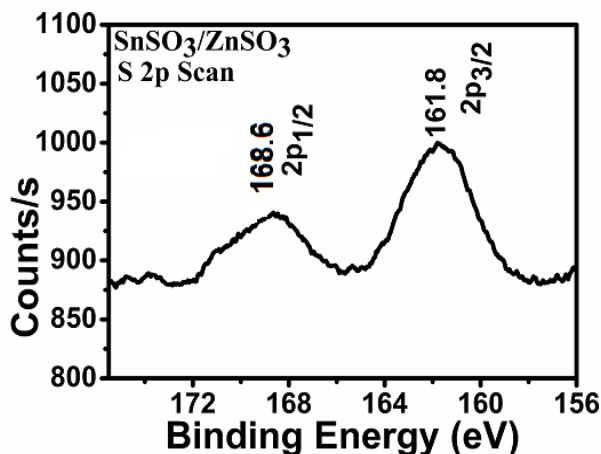


Fig. 7. Sulphur 3d scan of  $\text{SnSO}_3/\text{ZnSO}_3$ .

In the oxygen scan (Figure 8), the most noticeable peak appears at 531.1 eV. The oxygen 1s core level signal is represented by this peak. The innermost electron shell of oxygen atoms is denoted by "1s." The oxygen's chemical environment of the material can be inferred from the peak position. Oxides, hydroxides, and adsorbed species are examples of chemical states that display different oxygen 1s peaks. According to reports, metal oxide bonds show maxima at 529 and 530 eV [14]. The formation of a metal oxide bond, namely oxides of zinc and tin, is indicated by the oxygen 1s peak at binding energy 531.1 eV [21].

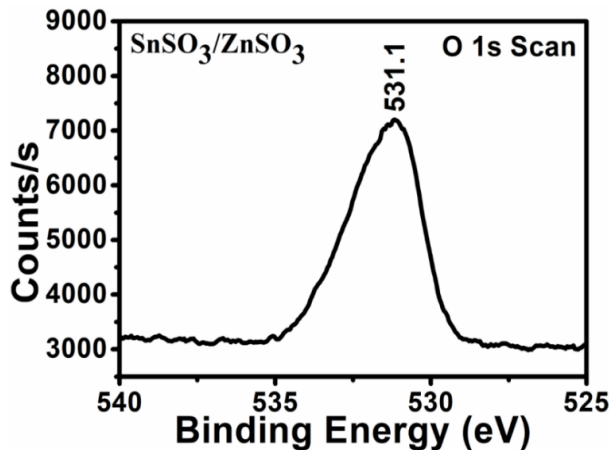


Fig. 8. Oxygen 1s scan of  $\text{SnSO}_3/\text{ZnSO}_3$ .

Survey spectrum shows presence of chemical and electronic state of the atoms within the element on the surface around 1-10 nm. The x-axis values of electron binding energy (eV) are shown against the y-axis values of total counts of detected electrons. It is utilized to identify any chemical element that exists within the top 10 nm of any surface [22]. Figure 9 depicts survey spectrum of  $\text{SnSO}_3/\text{ZnSO}_3$  nano composite. Peaks in the spectra are investigated and its corresponding chemical element along with its electronic state have been identified with reference to literature. First eminent peak at 24.5 eV corresponds to Sn with 4d electronic state [23]. At 283.1 eV, the peak corresponds to Zn 2p<sub>3/2</sub> [24]. Peaks at 487.0 and 495.8 eV of Sn 3d<sub>5/2</sub> and Sn 3d<sub>3/2</sub> provides evidence for spin-orbit splitting or j-j coupling with  $\Delta = 8.6$  which is consistent to the literature investigations [25]. The degeneracy or area ratio between the spin orbit splitting peaks of Sn element with j values 5/2 and 3/2 is determined by  $(2j+1)$ . It is found evident with the area ratio 3:2, which is denoting six electrons

in the 5/2 sub level and four electrons in the 3/2 sublevel of 3d shell [26]. Oxygen peak at 531.1 eV, is corresponding to 1s electronic state [27]. And the peaks at 713.7 and 757.4 eV is denoting Sn 3p<sub>3/2</sub> and Sn 3p<sub>1/2</sub> electronic states [23].

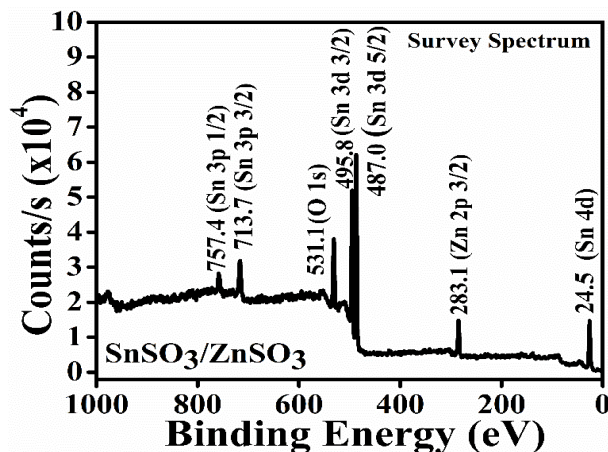


Fig. 9. XPS survey spectrum of SnSO<sub>3</sub>/ZnSO<sub>3</sub>.

### 3.6. Electrochemical performance in three electrode configurations

#### 3.6.1. Cyclic voltammetry (CV)

The cyclic voltammogram of SnSO<sub>3</sub>/ZnSO<sub>3</sub> nano composite shows a characteristic bell-shaped curve, as depicted in Figure 10, and an operational potential window of 1.6 V at different scan rates of 5 mV, 10 mV, 25 mV, 50 mV, 75 mV and 100 mV is observed. Specific capacitance of the nanocomposite derived from the CV plot are found to be 103.0 F/g, 80.9 F/g, 67.3 F/g, 60.8 F/g, 57.6 F/g and 55.2 F/g. Specific capacitance decreases with increased scan rate, as seen in Figure 11, due to the interaction between electrode and electrolyte [28-30].

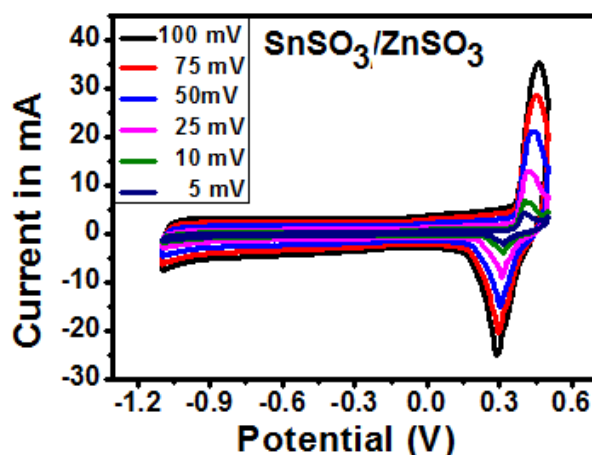


Fig. 10. CV curves of SnSO<sub>3</sub>/ZnSO<sub>3</sub>.

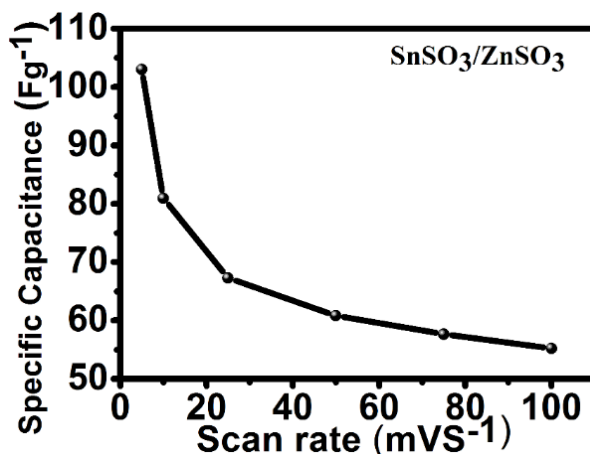


Fig. 11. Specific capacitance versus scan rate of SnSO<sub>3</sub>/ZnSO<sub>3</sub>.

The potential shift and peak currents act in accordance to the scan rate. Charge storage occurs by adsorption of cations in the electrolyte on an electrode surface. Electrostatic adsorption of ions causes oxidation peak potential to increase and reduction peak potential to decrease at various scan speeds of 5, 10, 25, 50, 75, and 100 mV/s. It is caused due to redox process that follows charge transfer movement. Because of deficient ion interaction into the dense core of the nanostructure, anodic peaks move to higher potential and cathodic peaks to lower potentials. The redox peak shift demonstrates the electrode material's high-rate capacity for use in supercapacitor systems [31]. Observing the curve's peaks, the anodic peak correlates to oxidation reaction, indicating loss of electron, and the cathodic peak corresponds to reduction reaction, showing gain of electron. The location of these peaks offers information about redox behavior of the material.

At slower scan rate, the process becomes diffusion-limited and regulated by mass transport. At faster scan rates, the process becomes kinetically constrained and regulated by reaction kinetics [32]. At slow scan rate, mass transport dominates the electrochemical process. The diffusion layer surrounding the electrode surface growing rapidly. As a result, flow of electrically charged ions or molecules reaching the electrode surface is significantly reduced. When the scan rate is slow, the reactants, which are ions or molecules, have enough time to diffuse to the electrode surface. Slower scan rates give more time for mass transfer or diffusion of ions or molecules to the surface of electrode. However, this longer duration does not necessarily result in increased capacitance [33]. The limiting aspect is their ability to proceed through the solution rapidly enough to reach the electrode. The slow diffusion of ions leads to a decreased charge storage capacity; however, the longer diffusion time permits ions to assemble near the electrode, increasing the effective amount of surface area for charge storage. As a result, the specific capacitance normalized by the surface area is often larger. The current response, or peak current, is exactly proportional to the rate of mass movement. Diffusion-limited processes frequently produce symmetrically well-defined and aligned peaks in CV curves. The system acts more like diffusion-limited domain. At high scan rates, the electrochemical mechanism is governed by reaction kinetics. At higher scan rates, the reactants do not have adequate time to diffuse through the electrolytic solution [34]. The thinner diffusion layer remains at rapid scan rates. There is an increase in the species flow to the electrode surface. Both the cathodic and anodic peak currents increase. Charge transfer kinetics are improved by faster scan rates. The system is more likely exists as kinetics-limited domain. Higher charge storage capacity is made possible by rapid electron transfer. However, the short duration for ion diffusion may cause the specific capacitance to drop. Rapid electron transport may provide the appearance of sharper peaks. The kinetics of the redox process now affect the current reaction of peak current [35].

### 3.6.2. Galvanostatic charge-discharge analysis (GCD)

Chronopotentiometry (CP) analysis of charging and discharging for  $\text{SnSO}_3/\text{ZnSO}_3$  in 3M KOH electrolyte at current densities 1, 2, 3, 4, 5, and 6 A/g is shown in Figure 12. The behaviour of pseudocapacitors is illustrated by quasi-triangular CP curves. As the current density rises, the electrode material's internal resistance increases [36-37].

Actually, the active surface area involved in electrode-electrolyte interactions is proportional to the material-specific capacitance.  $\text{SnSO}_3/\text{ZnSO}_3$  nanocomposite shows specific capacitances of 117.8, 83.8, 73.1, 68.4, 67.9 and 66.2 F/g for 1, 2, 3, 4, 5, and 6 A/g current densities in 3M electrolyte of KOH, respectively (Figure 13). The charge transfer kinetics take the spotlight at low current densities. Oxidation or reduction reactions at the electrode happen more slowly. This slow behaviour is reflected in the possible reaction. The importance of faradaic processes increases with increasing current density. Reversible redox processes exist at the electrode surface and the total capacitance is influenced by pseudo capacitance. Additional redox reactions take place if the supercapacitor material displays pseudo capacitance. The total capacitance is influenced by these faradaic processes [38]. In the event where pseudo capacitance is substantial, the slope might become more noticeable. At greater currents, these responses happen more quickly. The capacitance achieves an equilibrium level at a given voltage. The charge storage capacity is not appreciably increased by increasing the voltage. The contribution of Faradaic reactions saturates, and they have certain limits [39]. The equilibrium between ion diffusion and charge transfer causes the potential to get stabilized. At large currents, ion diffusion gets troublesome and the time it takes for the ions to reach the electrode surface is reduced. As a result, the rate at which charges are stored is limited by diffusion restrictions. When current densities are large, specific capacitance falls. This suggests that there are fewer activation sites for electrolytic ions at the electrode-electrolyte interface and a lack of ion trapping which is necessary for electrochemical behaviour [40].

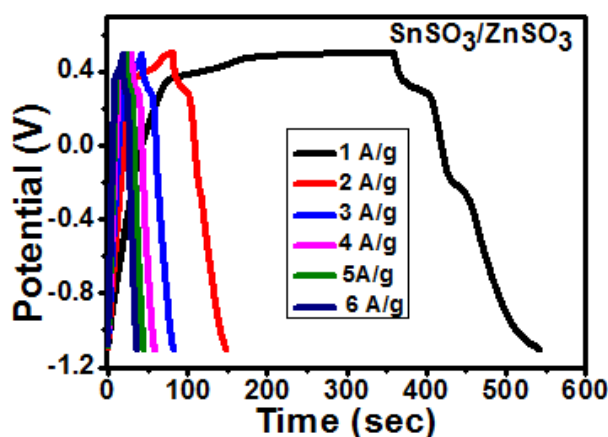


Fig. 12. GCD curves of  $\text{SnSO}_3/\text{ZnSO}_3$ .

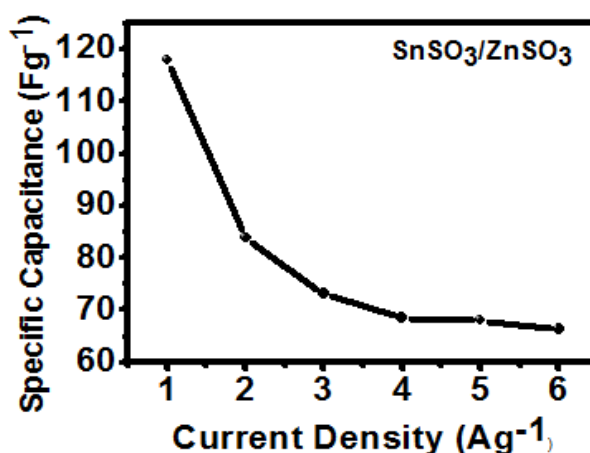


Fig. 13. Specific capacitance versus current density of  $\text{SnSO}_3/\text{ZnSO}_3$  from GCD.

### 3.6.3. Nyquist plot

A Nyquist plot for  $\text{SnSO}_3/\text{ZnSO}_3$  is shown in Figure 14, along with an extended plot as an inset. It confirms pseudo capacitor behavior by displaying a semicircle with the Warburg region continuing to extend. The charge-transfer process is shown by a very tiny semicircle. The charge transfer resistance is  $1.424 \Omega$ , and the series resistance  $R_s$  is low at  $0.9605 \Omega$ . An inset depicts the Randles circuit, which is the equivalent circuit model. When diffusion and kinetics are both significant, it can be applied to electrode processes. The charge transfer resistance, the solution resistance ( $R\Omega$ ), a pseudo capacitor ( $C$ ), and the Warburg element ZWAR, which provides information on the species' diffusion coefficient are all defined [41-44].

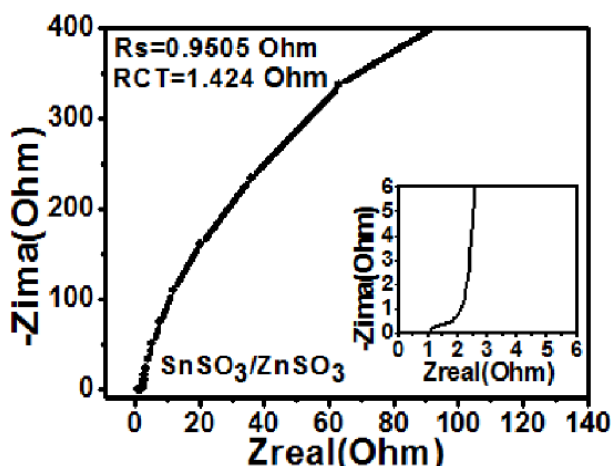


Fig. 14. Nyquist plot of  $\text{SnSO}_3/\text{ZnSO}_3$  in three electrode system.

## 4. Conclusions

$\text{SnSO}_3/\text{ZnSO}_3$  nanocomposite is synthesized by hydrothermal method. X-ray powder diffraction assures the perfect formation of  $\text{SnSO}_3/\text{ZnSO}_3$  nanocomposite. It reveals clear morphology of nail like nanorod structure. Thermal analysis illustrates the stability, decomposition behavior and critical temperatures where significant weight loss occurs. DTA Curve describes about the physical and chemical changes occurred in the nanocomposite due to presence of troughs at  $280^\circ$ ,  $322^\circ$ ,  $357^\circ$  and at  $410^\circ\text{C}$  and beyond  $500^\circ\text{C}$ , the nanocomposite decomposes rapidly. TGA response of the nanocomposite shows drastic change in its mass loss over frequent rise in the temperature. Nearly 27.1% mass loss is observed over  $995^\circ\text{C}$ . X-ray photoemission analysis describes the role of the chemical state of Zn, Sn, O and S in  $\text{SnSO}_3/\text{ZnSO}_3$ .

Electrochemical analysis in three electrode system is undergone. In three electrode system, voltammogram of  $\text{SnSO}_3/\text{ZnSO}_3$  nano composite, depicts a typical bell-shaped curve and exhibits an operational potential window of 1.6 V. The specific capacitance ( $C_s$ ) values from voltammogram are 103.0 F/g, 80.9 F/g, 67.3 F/g, 60.8 F/g, 57.6 F/g and 55.2 F/g for different scan rates 5 mV, 10 mV, 25 mV, 50 mV, 75 mV and 100 mV respectively. Chronopotentiometry (CP) analysis of charging and discharging depicts quasi-triangular curves, which explains the behavior of pseudo capacitors. Specific capacitances of 117.8, 83.8, 73.1, 68.4, 67.9 and 66.2 F/g were observed for 1, 2, 3, 4, 5 and 6 A/g current densities in 3M electrolyte of KOH, respectively, in  $\text{SnSO}_3/\text{ZnSO}_3$ . Nyquist plot for  $\text{SnSO}_3/\text{ZnSO}_3$  confirms pseudo capacitor behaviour. Series resistance ( $R_s$ ) found low that is,  $0.9505 \Omega$  and charge transfer resistance found as  $1.424 \Omega$ .

## Acknowledgments

Authors thank DST-FIST, Department of Physics, Gandhigram Rural Institute, Deemed To Be University, Gandhigram, Dindigul District, Tamilnadu, India for providing XRD facility.

## References

- [1] Francisco Fabregat-Santiago, Ivan Mora-Seró, Germà Garcia-Belmonte, Juan Bisquert, J. Phys. Chem. B, 107, 758 (2003); <https://doi.org/10.1021/nl0342390>
- [2] Marek Wojnicki, Marc Escrivà-Gelonch and Volker Hessel, Metals, 14, 1237 (2024); <https://doi.org/10.3390/met14111237>
- [3] <https://www.biologic.net/topics/what-is-cv-a-comprehensive-guide-to-cyclic-voltammetry/>
- [4] Tsierkezos, J Solution Chem 36, 289 (2007); <https://doi.org/10.1007/s10953-006-9119-9>
- [5] P. A. van Manen, R. Weewer, J. H. W. de Wit, Journal of The Electrochemical Society, 139, 1130 (1992); <https://doi.org/10.1149/1.2069352>
- [6] Lei Zhang, Xiaosong Hu, Zhenpo Wang, Fengchun Sun, David G. Dorrell, Renewable and Sustainable Energy Reviews, 81, 1868 (2018); <https://doi.org/10.1016/j.rser.2017.05.283>
- [7] <https://oqmd.org/materials/entry/1758603>
- [8] <https://oqmd.org/materials/structure/8413454>
- [9] <https://oqmd.org/materials/structure/8430483>
- [10] A. Modwi, K. K. Taha, L. Khezami, Zeitschrift für Physikalische Chemie, 235, 745 (2021); <https://doi.org/10.1515/zpch-2019-1473>
- [11] <http://www.ejpau.media.pl/volume11/issue2/art-25.html>
- [12] Aparicio, Gladis Medina-Vargas, Giovanni Díaz-Puentes, Edgar, Heliyon, 6, e05262 (2020); <https://doi.org/10.1016/j.heliyon.2020.e05262>
- [13] De la Fuente, José Luis Ruiz-Bermejo, Marta Salvan, Cesar Osuna-Esteban, Susana, Polymer Degradation and Stability, 96, 943 (2011); <https://doi.org/10.1016/j.polymdegradstab.2011.01.033>
- [14] John F. Moulder, William F. Stickle, Peter E. Sobol, Kennetlf D. Bomben, Edited by Jill Chastain, Handbook of X-Ray Photoelectron Spectroscopy, Perkin-Elmer Corporation, USA (1992).
- [15] <https://xpsdatabase.net/tin-sn-z50-tin-compounds/>
- [16] <https://xpsdatabase.com/zinc-zn-z30/>
- [17] Anshuman Sahai, Navendu Goswami, Ceramics International, 40, 14569 (2014); <https://doi.org/10.1016/j.ceramint.2014.06.041>
- [18] <https://xpsdatabase.net/sulfur-spectra-sulfur-natural-crystal/>
- [19] A.Fraga, C.Do, C.P.B.Quitete, V.L.Ximenes, E.F.Sousa-Aguiar, I.M. Fonseca, A.M.B.Rego, J. Mol. Catal. A Chem. 422, 248 (2016); <https://doi.org/10.1016/j.molcata.2015.12.005>
- [20] [https://www.frontiersin.org/files/Articles/529882/fchem-08-00263-HTML/image\\_m/fchem-08-00263-g003.jpg](https://www.frontiersin.org/files/Articles/529882/fchem-08-00263-HTML/image_m/fchem-08-00263-g003.jpg)
- [21] <https://sites.cardiff.ac.uk/xpsaccess/reference/oxygen/>
- [22] <https://xpsmetrology.com/surveyspectra/#:~:text=The%20survey%20spectrum%20reveals%20whatcounts%20Y%2Daxis%20values>
- [23] <https://xpsdatabase.net/tin-sn-z50-tin-compounds/>
- [24] <https://xpsdatabase.net/zinc-spectra-zn-metal/>
- [25] <https://www.thermofisher.com/in/en/home/materials-science/learning-center/periodic-table/other-metal/tin.html>
- [26] <https://www.harwellxps.guru/knowledgebase/spin-orbit-splitting/#:~:text=All%20orbitals%20except%20the%20s,also%20known%20as%20j%2Dj%20c>

oupling).

[27] [https://www.researchgate.net/figure/PS-spectra-of-oxygen-1s-in-high-resolution-spectra-a-NF-control-b-NF-40\\_fig5\\_342579603](https://www.researchgate.net/figure/PS-spectra-of-oxygen-1s-in-high-resolution-spectra-a-NF-control-b-NF-40_fig5_342579603)

[28] H. Gupta, S. Chakrabarti, S. Mothkuri, B. Padya, T. N. Rao, P. K. Jain, *Materials Today Proceedings*, 26, 20 (2020); <https://doi.org/10.1016/j.matpr.2019.04.198>

[29] V. Adimule, B.C. Yallur, M. Challa, R.S. Joshi, *Heliyon*, 7, e08541 (2021); <https://doi.org/10.1016/j.heliyon.2021.e08541>

[30] Gissawong, Netsirin Srijaranai, Supalax Boonchiangma, Suthasinee Uppachai, Pikaned Seehamart, Kompichit Jantrasee, Sakwiboon Moore, Eric Mukdasai, Siriboon, *Microchimica Acta*, 188, 208 (2021); <https://doi.org/10.1007/s00604-021-04869-z>

[31] S. Aripnammal, N.G. Basil Ralph, S. Shanmugha Soundare, R. Jayavel, *Nano*, 19, 2450021 (2024); <https://doi.org/10.1142/S1793292024500218>

[32] Badar, Waqas Ali, Husna Brooker, Olivia Newham, Elis Snow, Tim Terrill, Nicholas Tozzi, Gianluca Fratzl, Peter Knight, Martin Gupta, Himadri, *Plos One*, 17, e0273832 (2022); <https://doi.org/10.1371/journal.pone.0273832>

[33] Aranzales, D. Briliani, I. McCrum, I.T. Wijenberg, J.H.O.J. de Vooy, Arnoud Koper, Marc, *Electrochimica Acta*, 368, 137606 (2021); <https://doi.org/10.1016/j.electacta.2020.137606>

[34] [https://batch.libretexts.org/print/url=https://chem.libretexts.org/Bookshelves/Analytical\\_Chemistry/Supplemental\\_Modules\\_%28Analytical\\_Chemistry%29/Analytical\\_Sciences\\_Digital\\_Library/Courseware/Analytical\\_Electrochemistry%3A\\_The\\_Basic\\_Concepts/04\\_Voltammetric\\_Methods/A\\_Basics\\_of\\_Voltammetry/02\\_Potential\\_Sweep\\_Methods/b%29\\_Cyclic\\_Voltammetry/ii%29\\_Important\\_parameters\\_in\\_CV.pdf](https://batch.libretexts.org/print/url=https://chem.libretexts.org/Bookshelves/Analytical_Chemistry/Supplemental_Modules_%28Analytical_Chemistry%29/Analytical_Sciences_Digital_Library/Courseware/Analytical_Electrochemistry%3A_The_Basic_Concepts/04_Voltammetric_Methods/A_Basics_of_Voltammetry/02_Potential_Sweep_Methods/b%29_Cyclic_Voltammetry/ii%29_Important_parameters_in_CV.pdf)

[35] <https://www.nanoscience.com/techniques/electrochemistry/electrochemical-measurements-cyclic-voltammetry/>

[36] K.V. Sankar, D. Kalpana, R. K. Selvan, *Journal of Applied Electrochemistry*, 42, 463 (2012); <https://doi.org/10.1007/s10800-012-0424-2>

[37] B.J. Reddy, P. Vickraman, A.S. Justin, *Physica Status Solidi*. 216, 1800595 (2018); <https://doi.org/10.1002/pssa.201800595>

[38] Y. Ge, X. Xie, J. Roscher, Q. Qu. *Journal of Solid State Electrochemistry*, 24, 3215 (2020); <https://doi.org/10.1007/s10008-020-04804-x>

[39] S. Ratha, A.K. Samantara, *Characterization and Performance Evaluation of Supercapacitor*. In: *Supercapacitor: Instrumentation, Measurement and Performance Evaluation Techniques*. Springer Briefs in Materials. Springer, Singapore, 23 (2018); [https://doi.org/10.1007/978-981-13-3086-5\\_3](https://doi.org/10.1007/978-981-13-3086-5_3)

[40] <https://www.metrohm.com/content/dam/metrohm/shared/documents/application-notes/ans/AN-SC-001.pdf>

[41] B.A. Mei, O. Munteshari, J. Lau, B. Dunn, L. Pilon, *Journal of Physical Chemistry C*, 122, 194 (2018); <https://doi.org/10.1021/acs.jpcc.7b10582>

[42] [https://partners.metrohm.com/GetDocumentPublic?action=get\\_dms\\_document&docid=2043973](https://partners.metrohm.com/GetDocumentPublic?action=get_dms_document&docid=2043973).

[43] W. Choi, H. C. Shin, J. M. Kim, J. Y. Choi, W. S. Yoon, *Journal of Electrochemical Science and Technology*, 11, 1 (2020); <https://doi.org/10.33961/jecst.2019.00528>

[44] E.P.Randviir, C.E.Banks, *Analytical Methods*, 5, 1098 (2013); <https://doi.org/10.1039/c3ay26476a>